Journal of Computational Physics 546 (2026) 114477

Contents lists available at ScienceDirect

Journal of Computational Physics

journal homepage: www.elsevier.com/locate/jcp

Modal decomposition in numerical modelling of eddy current problems

Salvatore Ventre [a], Vincenzo Mottola [a], Nicola Isernia [b], Andrea Gaetano Chiariello [c,*], Antonello Tamburrino [a,d]

[a] *Dipartimento di Ingegneria Elettrica e dell'Informazione, Universita di Cassino e del Lazio Meridionale, Via Gaetano di Biasio 43, 03043, Cassino, Italy*
[b] *Dipartimento di Ingegneria Elettrica e delle Tecnologie dell'Informazione, Università degli Studi di Napoli Federico II, Via Claudio 21, 80125, Napoli, Italy*
[c] *Dipartimento di Ingegneria, Università degli Studi della Campania Luigi Vanvitelli, via Roma 29, 81031, Aversa, Italy*
[d] *EUTINN, European Research Institute, European University of Technology, Italy*

ARTICLE INFO

Keywords:
Eddy current computation
Eigenvalues
Modal decomposition
Integral equation
Finite element method
Magneto-quasi-stationary limit
Nondestructive testing
Eddy current testing

ABSTRACT

A methodology to reduce the computational cost of time domain computations of eddy currents problems is proposed. It is based on the modal decomposition of the current density. In particular, a convenient strategy to perform the modal decomposition even in presence of injected currents into the electrodes of a conducting domain is proposed and implemented in a parallel computing environment. Using a theta-method integration algorithm, the performances of the proposed approach are compared against those of a classical method based on the Cholesky factorization, for a case of interest in the framework of Eddy Current Nondestructive testing. For this large eddy current problem (number of unknowns greater than 100k, number of time steps of interest equal to 100k) the proposed solution method is shown to be much faster than those based on standard time integration schemes.

1. Introduction

In a variety of applications, ranging from the design of magnets of fusion devices or accelerators to non-destructive testing, it is necessary to perform long time-domain eddy currents simulations over very large or densely discretized conducting domains. The computation of eddy currents in bulk conductors for assigned induced or applied voltages from external sources is a standard engineering problem, which can be addressed by the means of integral formulations and finite element techniques [1–5]. After the discretization to a finite element space, the problem is equivalent to that of solving a linear system of Ordinary Differential Equations, possibly with holonomic constraints. In this framework, this contribution describes a modal decomposition approach for the simulation of constrained eddy current problems, together with the conditions which make such approach convenient.

Non-destructive testing techniques, based on eddy currents, are very common and widespread, since they have been proven to be effective both for non-destructive evaluation [6,7] and for tomographic applications [8]. Generally, an eddy current system for non-destructive evaluation consists of a set of coils able to induce eddy currents in the specimen under test and to measure the reaction magnetic field produced by the latter. One of the main advantages of this configuration is the possibility to perform contactless measurements and in-line/on-line inspections following the route designed by the paradigm of Industry 4.0 [9]. However, there are

* Corresponding author.
E-mail address: andreagaetano.chiariello@unicampania.it (A.G. Chiariello).

https://doi.org/10.1016/j.jcp.2025.114477
Received 11 October 2024; Received in revised form 13 October 2025; Accepted 20 October 2025
Available online 5 November 2025

Table 1
Notation adopted throughout the article.

a	discrete vector (1D array)
$\mathbf{A}$	discrete matrix (2D array)
$\mathbf{a}(\mathrm{x})$	vector field in Euclidean three-dimensional space
$\langle A, B\rangle$	Euclidean scalar product between scalar or vector fields in $L_2(\Omega)$
$\langle A, B\rangle_{\Sigma_k}$	scalar product on Σ_k
$\mathcal{A}$	Linear operator $H_L(\Omega, \partial\Omega) \to L_2(\Omega, \mathbb{R}^3)$ defined by (7)
$\mathcal{I}$	Linear operator $H_L(\Omega, \Sigma) \to \mathbb{R}^{N_e}$ defined by (14)

specific applications where variants of this contactless method provide a valuable option as, for instance, in the inspection of oil and gas pipelines.

In the case of long pipelines, a relatively new technique has been recently proposed [10,11]. This approach requires to directly inject alternating currents into the specimen under test (SUT) by means of proper conductors located at, potentially, long distances (of the order of kilometers) [12], and to measure the resulting magnetic flux density even relatively far away from the pipe (at most 2 m) [12]. The direct current injection gives, also, the possibility to operate on a wider range of frequency, from quasi direct currents to hundreds of kHz [11], and, hence, to detect both inner and outer defects in the pipe, being the eddy currents capable of fully penetrating the specimen.

The AC Current Potential Drop (ACPD) is another variant of the method, also widely employed in this scenario. It consists in a four points measurement, in which two electrodes are used to inject an alternating current into the specimen while the remaining two electrodes measure a voltage drop. The voltage drop can be related to the thickness, the electrical conductivity or to the presence of flaws in the specimen [13–15]. The ACPD has been successfully applied to monitor crack growth [16] and creep strain [17] in steel and to infer stress [18], showing better performances and reliability then other non-destructive techniques, in addition to the capability to be employed in-line inspections.

For both the two discussed methods, numerical simulations plays a fundamental role for different reasons. Indeed, (i) numerical simulations are the key tool in the design and development of inspection systems, allowing to optimize the design parameters to achieve better overall performances, (ii) numerical simulations are essential in the solution of the inverse problem, i.e. retrieving the unknown parameters of the specimen under test, since they represent a vital block for any iterative scheme [19], (iii) the possibility to numerically simulate the magnetic response in the presence of different flaws allows to build a database of signals for a large variety of different defect for shape, position and dimension that can be used in implementing metrics performance for non-destructive evaluation techniques [11]. However, numerical simulations in this context pose some challenges. Indeed, a proper inspection (see Section 4) may requires measurements at either (i) many different frequencies at the same time, or (ii) in the time domain for long transient. In other words, there is a need of fast electromagnetic solver specifically tailored for this kind of scenario.

Modal decomposition of eddy current problems has found applications both in the field of imaging and material characterization [8], and of the plasma-wall interaction studies in magnetic confinement fusion devices [20,21]. Those applications focus on the solution of specific problems after their approximation by proper finite element techniques and do not consider the possibility of having injected currents. Recently, in the absence of impressed currents, it was shown rigorously that a modal decomposition of the eddy current problem into an infinite countable set of eigenmodes is always possible for bounded domains [22]. The related eigenvalues can be ordered in descending order, providing useful indications on how to approximate the solution via a finite set of basis functions.

This paper proposes a theoretical contribution on the existence of a modal decomposition for eddy current problems in a general setting, which is then translated into a highly efficient numerical method for speeding up the associated numerical computations. First we show how some of the results presented in [22] can be extended to the case where injected currents into conductors are also present. This is relevant both for the inspection of pipes via some non-destructive-evaluation techniques and for the analysis of halo currents generated during disruptions of tokamak experiments. Hence, the attention is devoted to the possibility of representing the exact solution of the continuum eddy current problem as a linear combination of a countable set of eigenmodes, even in the presence of injected currents through electrodes placed on the boundary of the conducting domain. Those considerations are consequently translated to the discrete context, after the approximation of an integral formulation of the eddy current problem by means of an finite element technique. The modal approach is embedded in the numerical method with reference to problems where the required accuracy makes a direct solver mandatory. Indeed, in these cases, the computational cost to factorize the stiffness matrix ("classical" approach) and that for evaluating the modal decomposition are comparable ($N^3/3$ vs. $11N^3/3$). This makes the modal decomposition a key numerical tool for reducing the computational cost in transients where a "large" number of time-steps is required, as is the case for long transients and/or stiff problems, and/or driving signals with large bandwidth. Indeed, in these cases, the modal decomposition is more efficient than evaluating a backsubstitution at each time step (the classical approach). Dedicated examples from eddy current testing will allow us to provide indications on when and why it is convenient to perform a modal decomposition of the original problem in treating large constrained and unconstrained eddy current simulations, rather than resorting to classic numerical integration schemes.

The paper is organized as follows: in Section 2 the mathematical model is detailed and the modal decomposition for the eddy current problem in the presence of electrodes is derived, in Section 3 the numerical model is formulated, and in Section 4 a realistic numerical example for the non-destructive testing of a pipe is reported, where a transient problem is analyzed in the presence of multi-frequency driving, comparing performances of the proposed method to the other existing numerical techniques. Finally, in Section 5, conclusions are drawn.

2. Modal decomposition of the eddy current density

2.1. Notations and functional spaces

Throughout this paper, Ω is the region occupied by the conducting material. We assume $\Omega \subset \mathbb{R}^3$ to be an open connected bounded domain, with a Lipschitz boundary and outer unit normal $\hat{\mathbf{n}}$. We denote by V and S the 3-dimensional and the bi-dimensional Hausdorff measure in $\mathbb{R}^3$, respectively and by $\langle \cdot, \cdot \rangle$ the usual L^2-integral product on Ω. (Refer to **List of symbols and conventions** in Table 1).

Hereafter we refer to the following functional spaces

$$L^\infty_+(\Omega) := \{\theta \in L^\infty(\Omega) \mid \theta \geq c_0 \text{ a.e. in } \Omega \text{ for } c_0 > 0\}, \tag{1}$$

$$H_{\text{div}}(\Omega) := \{\mathbf{v} \in L^2(\Omega; \mathbb{R}^3) \mid \text{div}(\mathbf{v}) \in L^2(\Omega)\}, \tag{2}$$

$$H_{\text{curl}}(\Omega) := \{\mathbf{v} \in L^2(\Omega; \mathbb{R}^3) \mid \text{curl}(\mathbf{v}) \in L^2(\Omega)\}, \tag{3}$$

$$H_L(\Omega) := \left\{\mathbf{v} \in H_{\text{div}}(\Omega) \mid \text{div}(\mathbf{v}) = 0 \text{ in } \Omega,\ \mathbf{v} \cdot \hat{\mathbf{n}} = 0 \text{ on } \partial\Omega\right\}, \tag{4}$$

$$H_L(\Omega, \Sigma) := \left\{\mathbf{v} \in H_{\text{div}}(\Omega) \mid \text{div}(\mathbf{v}) = 0 \text{ in } \Omega,\ \mathbf{v} \cdot \hat{\mathbf{n}} = 0 \text{ on } \partial\Omega \backslash \Sigma\right\}, \tag{5}$$

and to the derived spaces $L^2(0, T; H_L(\Omega))$, $L^2(0, T; H_L(\Omega, \Sigma))$ and $L^2(0, T; H_{\text{curl}}(\Omega))$, for any $0 < T < +\infty$.

It is worth noting that $H_L(\Omega)$ is required to account for vector fields that cannot enter/leave the domain Ω, whereas $H_L(\Omega, \partial\Omega)$ is required to account for vector fields that can enter/leave the domain Ω through the entire $\partial\Omega$. Finally, $H_L(\Omega, \Sigma)$ is required to account for vector fields that can leave the domain Ω *only* through surface Σ (see Fig. 1). Moreover,

$$H_L(\Omega) = H_L(\Omega, \emptyset) \subset H_L(\Omega, \Sigma) \subset H_L(\Omega, \partial\Omega).$$

We refer to [23,24] for $H_L(\Omega)$ and a general discussion on functional spaces related to Maxwell equations.

2.2. Mathematical model for the eddy current problem

The eddy current problem, corresponding to Maxwell's equation in the Magneto-Quasi-Stationary limit (see [25]), can be cast in several different manners. Among them, an interesting formulation is that proposed by A. Bossavit (see [24]) consisting in the following integral formulation in the weak form:

$$\langle \eta \mathbf{j}, \mathbf{w} \rangle + \langle \partial_t \mathcal{A} \mathbf{j}, \mathbf{w} \rangle = -\langle \partial_t \mathbf{a}_S, \mathbf{w} \rangle \quad \forall \mathbf{w} \in H_L(\Omega), \tag{6}$$

where $\eta \in L^\infty_+(\Omega)$, $\mathbf{j} \in L^2(0, T; H_L(\Omega))$ is the unknown induced current density, Ω is the region occupied by the conducting material, $\mathcal{A}$ is the compact, self-adjoint, positive definite operator:

$$\mathcal{A} : \mathbf{v} \in H_L(\Omega, \partial\Omega) \mapsto \frac{\mu_0}{4\pi} \int_\Omega \frac{\mathbf{v}(x')}{||x - x'||} \, \mathrm{d}V(x') \in L^2(\Omega; \mathbb{R}^3), \tag{7}$$

$\eta \in L^\infty_+(\Omega)$ is the electrical resistivity, μ_0 is the free space magnetic permeability, $\mathbf{a}_S \in L^2(0, T; H_{\text{curl}}(\Omega))$ is the vector potential produced by the prescribed source current $\mathbf{j}_S \in L^2(0, T; H_L(\Omega_S))$, Ω_S is a bounded open set with Lipschitz boundary that is electrically insulated from Ω.

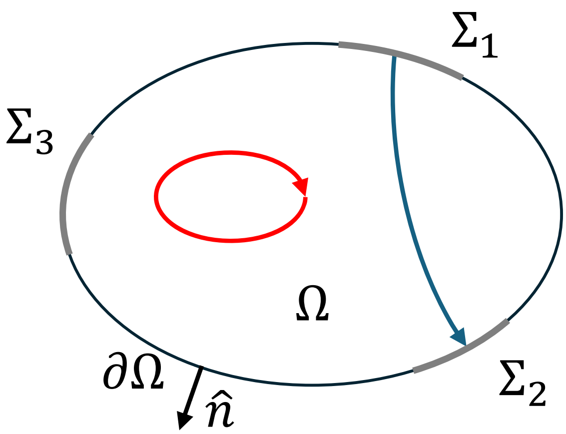

Fig. 1. Example of possible electrical current densities flowing in Ω.

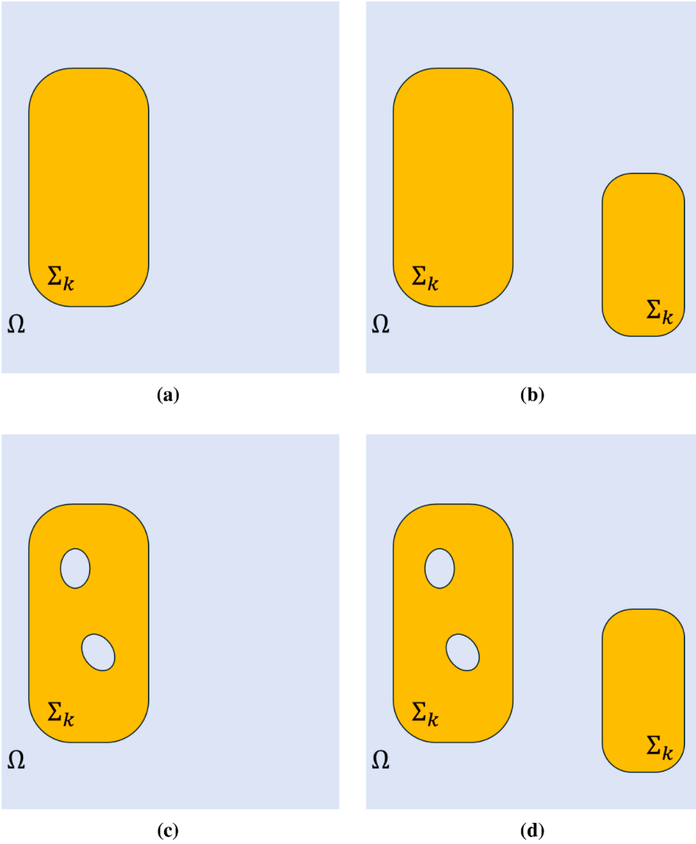

Fig. 2. Possible geometries for surface Σ_k (a) simply connected, (b) different simply connected components, (c) single connected component that is not simply connected, (d) different connected components that may be simply connected or not.

Remark 2.1. The integral formulation of (6) can be easily understood by combining (i) the constitutive relationship $\mathbf{e} = \eta\mathbf{j}$, (ii) the electric field expressed in terms of vector and scalar potential as $\mathbf{e} = -\partial_t\mathbf{a} - \partial_t\mathbf{a}_S - \nabla\phi$, being $\mathbf{a}$ the vector potential due to the induced current density $\mathbf{j}$ and ϕ the total scalar potential, and (iii) the vector potential due to the eddy current density expressed as $\mathbf{a} = \mathcal{A}\mathbf{j}$:

$$\eta\mathbf{j} + \partial_t\mathcal{A}\mathbf{j} + \nabla\phi = \partial_t\mathbf{a}_S \quad \text{in } \Omega, \tag{8}$$

The vector potential in (7) is selected according the Coulomb's gauge. The Magneto-Quasi-Stationary approximation dictates the choice of the functional space ($H_L(\Omega)$) and causes propagation to be neglected in the kernel of the operator $\mathcal{A}$.

It is worth noting that (6) models the physical situation when $\partial\Omega$, the boundary of the conducting domain, is in contact with an electrical insulator, indeed $\mathbf{j}\cdot\hat{\mathbf{n}} = 0$ on $\partial\Omega$ since $\mathbf{j} \in H_L(\Omega)$. A situation of relevant interest, which is the main focus of this contribution, is when electrical currents can flow through $\partial\Omega$ via a set of N_e boundary electrodes. Let $\Sigma_k \subset \partial\Omega$, $k = 1,\dots,N_e$ be the surface representing the k−th electrode. The Surface Σ_k is assumed to consist of a finite number of connected components, each connected component may be either simply connected or multiply connected, and the boundary of each connected component is Lipschitz (see Fig. 2). The electric current density $\mathbf{j}$ is an element of $L^2(0,T;H_L(\Omega,\Sigma))$ where $\Sigma = \bigcup_{k=1}^{N_e}\Sigma_k$. If, in addition, (i) the electrodes are made by a perfect conducting material and (ii) the net current through each electrode is imposed and equal to $i_k(t)$, the equivalent of (6), obtained from (8) written in the weak form, is

$$\langle\eta\mathbf{j},\mathbf{w}\rangle + \langle\partial_t\mathcal{A}\mathbf{j},\mathbf{w}\rangle + \sum_{k=1}^{N_e-1}\phi_k\langle 1,\mathbf{w}\cdot\hat{\mathbf{n}}\rangle_{\Sigma_k} = -\langle\partial_t\mathbf{a}_S,\mathbf{w}\rangle \quad \forall\mathbf{w}\in H_L(\Omega,\Sigma) \tag{9}$$

$$\langle 1,\mathbf{j}\cdot\hat{\mathbf{n}}\rangle_{\Sigma_k} = i_k^D \quad k = 1,\dots,N_e-1, \tag{10}$$

being $\mathbf{j}\in L^2(0,T;H_L(\Omega,\Sigma))$. In (9) it has been exploited that (i) implies the scalar potential to be constant on each electrode, whereas (ii) implies the constraint (10). In (9) and (10), we assumed the N_e−th electrode to be grounded, i.e. $\phi_{N_e} = 0$. It is worth noting that the ϕ_k's are unknown functions of the time and $i_{N_e}^D = -i_1^D - \dots - i_{N_e-1}^D$ because Ω is connected.

Remark 2.2. The linear functional:

$$\mathcal{I}_k : \mathbf{w}\in H_L(\Omega,\Sigma) \mapsto -\langle 1,\mathbf{w}\cdot\hat{\mathbf{n}}\rangle_{\Sigma_k} = -\int_{\Sigma_k}\mathbf{w}\cdot\hat{\mathbf{n}}\,\mathrm{d}S \in \mathbb{R} \tag{11}$$

gives the net electrical current entering Ω through the $k-$th electrode Σ_k and due to $\mathbf{w}$.

An effective approach to pose problem (9), (10) consists in decomposing $H_L(\Omega,\Sigma)$ in terms of an orthogonal direct sum:

$$H_L(\Omega,\Sigma) = H_0 \oplus H_D, \tag{12}$$

where

$$H_0 = \left\{ \mathbf{u} \in H_L(\Omega,\Sigma) \,|\, \langle 1, \mathbf{u}\cdot\hat{\mathbf{n}}\rangle_{\Sigma_k} = 0,\ k = 1,\dots,N_e \right\}, \tag{13}$$

and $H_D = H_0^{\perp}$. We notice that, $\forall \mathbf{u} \in H_D$ two or more terms of the type $\langle 1, \mathbf{u}\cdot\hat{\mathbf{n}}\rangle_{\Sigma_k}$ are non vanishing.

Remark 2.3. It is worth noting that H_0 represents solenoidal vector fields which do not correspond to a net circulation of electrical currents among the electrodes placed on the boundary of Ω. Similarly, H_D represents solenoidal vector fields corresponding to a net circulation of electrical currents among the electrodes.

It results that $\dim\left(H_D\right) = N_e - 1$, as from the following proposition.

Proposition 2.4. If Ω is a domain and on its boundary $\partial\Omega$ there are N_e electrodes/ports $\Sigma_1,\dots,\Sigma_{N_e}$, then $\dim\left(H_D\right) = N_e - 1$.

Proof. First, we notice that $H_0 = \ker(\mathcal{I})$, where $\mathcal{I}$ is the operator giving the net electrical current entering the electrodes/ports $\Sigma_1,\dots,\Sigma_{N_e}$

$$\mathcal{I} : \mathbf{w} \in H_L(\Omega,\Sigma) \mapsto \begin{bmatrix} \mathcal{I}_1\mathbf{w} \\ \vdots \\ \mathcal{I}_{N_e}\mathbf{w} \end{bmatrix} \in \mathbb{R}^{N_e}. \tag{14}$$

Then, we notice that $\dim(\mathrm{im}(\mathcal{I})) = N_e - 1$. Indeed, since Ω is assumed to be a domain (a non-empty connected open set), it results that $\sum_{k=1}^{N_e} \mathcal{I}_k\mathbf{w} = \int_{\partial\Omega} \mathbf{w}\cdot\hat{\mathbf{n}}\mathrm{d}S = 0$, via a divergence Theorem. This proves that the dimension of the preimage of $\mathrm{im}(\mathcal{I})$ under $\mathcal{I}$ is equal to $N_e - 1$.

The conclusions follows by recognizing that the latter, the preimage of $\mathrm{im}(\mathcal{I})$ under $\mathcal{I}$, coincides with H_D. $\square$

From (12) and Proposition 2.4 it follows that an arbitrary element of $H_L(\Omega,\Sigma)$ can be decomposed as:

$$\mathbf{w}(x) = \sum_{k=1}^{N_e-1} w_k^D \mathbf{s}_k^D(x) + \mathbf{w}_0(x), \tag{15}$$

where $\left\{\mathbf{s}_1^D,\dots,\mathbf{s}_{N-1}^D\right\}$ forms a basis of H_D and $\mathbf{w}_0 \in H_0$.

This decomposition induces a similar one on $L^2(0,T;H_L(\Omega,\Sigma))$, that gives the unknown $\mathbf{j}$ to be represented as

$$\mathbf{j}(x,t) = \mathbf{j}_D(x,t) + \mathbf{j}_0(x,t) = \sum_{k=1}^{N_e-1} \alpha_k^D(t)\mathbf{s}_k^D(x) + \mathbf{j}_0(x,t), \tag{16}$$

being $\mathbf{j}_0 \in L^2(0,T;H_0)$.

Decomposition (16) allows to solve constraint (10) easily. Indeed, when plugging (16) in (10) one has

$$\mathbf{F}\,\boldsymbol{\alpha}^{\mathbf{D}}(t) = \mathbf{i}_D(t) \tag{17}$$

where $\boldsymbol{\alpha}^D(t) = \left[\alpha_1^D(t),\dots,\alpha_{N_e-1}^D(t)\right]^T$, $\mathbf{i}_D(t) = \left[i_1^D(t),\dots,i_{N_e-1}^D(t)\right]^T$ and the matrix $\mathbf{F} \in \mathbb{R}^{(N_e-1)\times(N_e-1)}$ is defined as:

$$F_{kl} = \mathcal{I}_k\mathbf{s}_l^D = \langle 1, \mathbf{s}_l^D(x)\cdot\hat{\mathbf{n}}\rangle_{\Sigma_k}. \tag{18}$$

Since $\mathbf{F}$ is a full rank matrix, the solution of (17) is:

$$\boldsymbol{\alpha}^{\mathbf{D}}(t) = \mathbf{F}^{-1}\mathbf{i}_D(t). \tag{19}$$

At this stage, $\mathbf{j}_D$ is known and constraint (10) is satisfied. The equation for $\mathbf{j}_0$ comes by imposing (9) in H_0 rather than in $H_L(\Omega,\Sigma)$. By doing this, it turns out that

$$\langle \eta\mathbf{j}_0, \mathbf{w}\rangle + \langle \partial_t\mathcal{A}\mathbf{j}_0, \mathbf{w}\rangle = -\langle \eta\mathbf{j}_D, \mathbf{w}\rangle - \langle \partial_t\mathcal{A}\mathbf{j}_D, \mathbf{w}\rangle - \langle \partial_t\mathbf{a}_S, \mathbf{w}\rangle \quad \forall\mathbf{w} \in H_0, \tag{20}$$

where $\mathbf{j}_0 \in L^2(0,T;H_0)$. Eq. (20), together with (19), is the governing equation for this contribution.

Remark 2.5. In the weak formulation (9) or its equivalent (20), it is convenient to split the source vector potentials in two terms: a first term $\mathbf{a}_D$ devoted to the *direct* driving of electrical currents in the conducting domain Ω and another term $\mathbf{a}_E$ accounting for external electrical currents densities that are not entering into Ω, i.e. $\mathbf{a}_S = \mathbf{a}_D + \mathbf{a}_E$ (see Fig. 3).

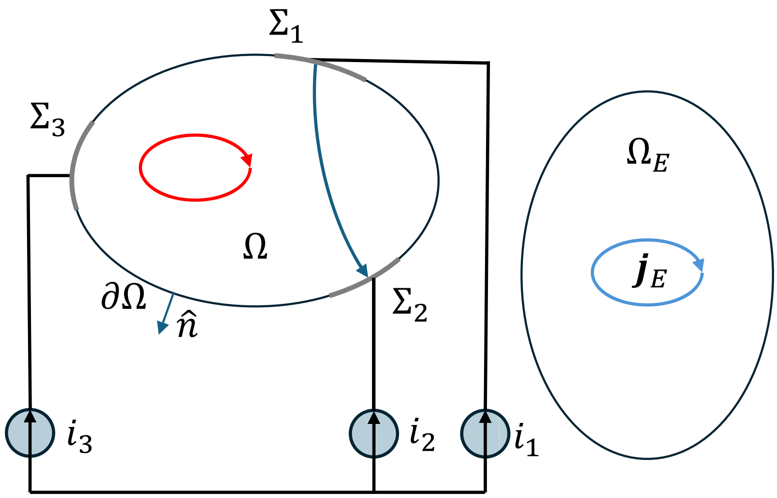

Fig. 3. Example of electrical currents external to Ω, either applied through the boundary electrodes (i_1, i_2, i_3) or circulating in the external region Ω_E. Notice that $i_1 + i_2 + i_3 = 0$ and that $\mathbf{j}_E$ produces the vector potential $\mathbf{a}_E$.

2.3. Modal decomposition

The modal decomposition for eddy current problems has been introduced and developed in [22] for problem (6).

The modal decomposition follows from space/time separation of variables applied to the source free problem. This is a key point to extend the results in [22] related to the modal decomposition for (6) (absence of boundary electrodes), to the eddy current problem in the presence of injected electrical current via a set of boundary electrodes, as described in (20) and (19). Indeed, by zeroing *all* source terms, problems (6) and (20) become

$$\langle \eta \mathbf{j}, \mathbf{w} \rangle + \langle \partial_t \mathcal{A} \mathbf{j}, \mathbf{w} \rangle = 0, \quad \forall \mathbf{w} \in H_L(\Omega) \tag{21}$$

$$\langle \eta \mathbf{j}_0, \mathbf{w} \rangle + \langle \partial_t \mathcal{A} \mathbf{j}_0, \mathbf{w} \rangle = 0, \quad \forall \mathbf{w} \in H_0, \tag{22}$$

where $\mathbf{j} \in L^2(0,T;H_L(\Omega))$ and $\mathbf{j}_0 \in L^2(0,T;H_0)$. It is clear that the problems giving rise to the modal decomposition in the absence of boundary electrodes (see (21)) or in the presence of boundary electrodes (see (22)) are similar and, indeed, they differ only for the underlying functional space that is $L^2(0,T;H_L(\Omega))$ and $L^2(0,T;H_0)$, respectively. Luckily, the change of functional space has a minor impact and it is possible to prove that all the results developed for modal decomposition for problem (21) (see [22]) can be extended to the problem (22). Here, for the sake of completeness, we briefly summarize the key findings.

Modal Decomposition

The solution of problem (20) can be expanded in terms of a Fourier series as

$$\mathbf{j}_0(x,t) = \sum_{n=1}^{\infty} i_n(t)\, \mathbf{j}_n(x) \quad \text{in } \Omega \times [0,T], \tag{23}$$

where $i_n \in L^2(0,T)$ and $\{\mathbf{j}_n\}_{n=1}^{+\infty}$ is the set of modes. In other terms, we have the following fundamental decomposition

$$L^2\left(0,T;H_0\right) = \overline{L^2(0,T) \otimes H_0}. \tag{24}$$

By combining (24), that $\left\{\mathbf{s}_1^D, \dots, \mathbf{s}_{N-1}^D\right\}$ forms a basis of H_D and (12), it results that

$$L^2\left(0,T;H_L(\Omega,\Sigma)\right) = \overline{L^2(0,T) \otimes H_L(\Omega,\Sigma)}. \tag{25}$$

A Generalized Eigenvalue Problem

The modes, and the related eigenvalues, are the solutions in H_0 of the following generalized eigenvalue problem:

$$\langle \mathcal{A}\mathbf{j}, \mathbf{w} \rangle = \tau(\eta) \langle \eta \mathbf{j}, \mathbf{w} \rangle \quad \forall\ \mathbf{w} \in H_0. \tag{26}$$

Properties of the modes and eigenvalues

1. the generalized eigenvalues and eigenvectors form countable sets: $\left\{\tau_n(\eta)\right\}_{n\in\mathbb{N}}$ and $\left\{\mathbf{j}_n\right\}_{n\in\mathbb{N}}$;
2. the set of eigenvectors $\{\mathbf{j}_n\}_{n\in\mathbb{N}}$ forms a complete basis in H_0;
3. The elements $\mathbf{j}_n$ are orthogonal with respect to η, i.e. $\langle \mathbf{j}_n, \eta \mathbf{j}_m \rangle = 0 \quad \forall\ n \neq m$;
4. The elements $\mathbf{j}_n$ are orthogonal with respect to $\mathcal{A}$, i.e. $\langle \mathbf{j}_n, \mathcal{A}\mathbf{j}_m \rangle = 0 \quad \forall\ n \neq m$;

5. the eigenvalues can be ordered such that $\tau_n(\eta) \geq \tau_{n+1}(\eta)$;
6. $\tau_n(\eta) > 0$ and $\lim_{n\to+\infty} \tau_n(\eta) = 0$;
7. the following max-min variational characterization of $\tau_n(\eta)$ holds:

$$\tau_n(\eta) = \max_{\dim(U)=n} \min_{\mathbf{j}\in U} \frac{\langle \mathcal{A}\mathbf{j}, \mathbf{j}\rangle}{\langle \eta\mathbf{j}, \mathbf{j}\rangle}, \tag{27}$$

where U is a linear subspace of H_0;
8. the eigenvalues satisfies a Monotonicity Principle w.r.t. the electrical resistivity η:

$$\eta_1 \leq \eta_2 \text{ a.e. in } \Omega \quad \Longrightarrow \quad \tau_n(\eta_1) \geq \tau_n(\eta_2)\ \forall n \in \mathbb{N},$$

where $\eta_1, \eta_2 \in L^\infty_+(\Omega)$, $\tau_n(\eta_1)$ and $\tau_n(\eta_2)$ are the n–th eigenvalues related to η_1 and η_2, respectively;

Decoupling the Eddy Current Problem

Once the modes $\{\mathbf{j}_n\}_{n\in\mathbb{N}}$ have been computed for a given electrical resistivity η, the eddy current density is determined from the i_ns. The evolution of these functions of the time is determined by the following *first order linear* ODE:

$$l_n i_n' + r_n i_n = \mathcal{E}_n^D + \mathcal{E}_n^S \quad \forall n \in \mathbb{N}. \tag{28}$$

In (28)

$$r_n = \langle \eta\mathbf{j}_n, \mathbf{j}_n\rangle, l_n = \langle \mathcal{A}\mathbf{j}_n, \mathbf{j}_n\rangle \tag{29}$$

$$\mathcal{E}_n^D = -\langle \eta\mathbf{j}_D, \mathbf{j}_n\rangle - \langle \partial_t\mathcal{A}\mathbf{j}_D, \mathbf{j}_n\rangle \tag{30}$$

$$\mathcal{E}_n^S = -\langle \partial_t\mathbf{a}_S, \mathbf{j}_n\rangle. \tag{31}$$

Hereafter we assume the unit of i_n to be that of an electrical current (A), in the International System of Units (SI). The unit of $\mathbf{j}_n$ is, therefore, the inverse of an area (m^{-2}), the unit of r_n is electrical resistance (Ω), the unit of l_n is henry (H), and the unit of $\mathcal{E}_n^D$ and $\mathcal{E}_n^S$ is volt (V).

Eq. (28) is the key to fast solution of eddy current problems: once the modes $\{\mathbf{j}_n\}_{n\in\mathbb{N}}$ are available, the computation of the i_ns is modeled by decoupled ODEs. Their solution can be computed (i) separately, (ii) with different integration methods, (iii) in a parallel environment, and (iv) in a selective manner.

It is worth noticing that, due to property 6 of the modes and eigenvalues, Eq. (28) is stable.

3. Modal decomposition in the discrete setting

This Section is devoted to the translation of the results and properties discussed in previous Section for the continuum model, to a discrete context where an approximate solution is sought in a finite-dimensional subspace of $H_L(\Omega,\Sigma)$. First the approximation of the problem to a finite-dimensional version is discussed in Section 3.1. The implications of the properties of modes and eigenvalues discussed in the continuum framework on the finite approximation are then specified in Section 3.2.

3.1. Discrete model

Eq. (25) reveals that the solution of the constrained eddy current problem (9)–(10) can be regarded as an infinite sum of factorized terms:

$$\mathbf{j}(x,t) = \sum_{n=1}^{\infty} i_n(t)\,\mathbf{j}_n(x) \quad \text{in } \Omega\times[0,T], \tag{32}$$

where $i_n(t) \in L^2(0,T)$ and $\mathbf{j}_n(x) \in H_L(\Omega,\Sigma)$ for each $n \in \mathbb{N}^+$. This allows to interpret the standard Galerkin approximation of problem (9)–(10) in terms of a truncation of the series (32):

$$\mathbf{j}(x,t) = \sum_{k=1}^{N} i_k(t)\mathbf{w}_k(x), \tag{33}$$

where $\{\mathbf{w}_k(x) \in H_L(\Omega,\Sigma),\ k = 1,\dots,N\}$ is a discrete set of basis functions and the i_ks are the related degrees of Freedom.

Clearly

$$X = \mathrm{span}\{\mathbf{w}_1,\dots,\mathbf{w}_N\} \tag{34}$$

is a vector subspace of $H_L(\Omega,\Sigma)$ of finite dimension, which shall be constructed conveniently, e.g. introducing a discretization and a finite element approximation of the problem.

Exactly as in the continuum model, it is convenient to introduce an orthogonal decomposition to distinguish between currents internal to the conducting domain and currents associated to net fluxes through electrodes. In different words, we are looking for the discrete analog of decomposition (12), i.e.

$$X = X_0 \oplus X_D, \tag{35}$$

where X_0 is the discrete approximation of H_0, *i.e.*

$$X_0 = \{\mathbf{v}(x) \in X \mid \langle 1, \mathbf{v}(x) \cdot \hat{\mathbf{n}} \rangle_{\Sigma_k} = 0 \quad \forall k = 1, \ldots, N_e\}, \tag{36}$$

and $X_D = X_0^{\perp}$. In doing this, it must be guaranteed that the $\mathbf{w}_k$s are such that the dimension of the linear space X_D is equal to $N_e - 1$, i.e. that it is possible to represent all the possible configurations with net electrical currents entering the domain Ω through the electrodes.

A convenient way of introducing a finite set of basis functions in $H_L(\Omega, \Sigma)$ is to discretize the conducting domain Ω with polyhedra and then introduce basis functions associated to mesh edges [1]. A tree-cotree decomposition reveals immediately which basis functions are linearly independent and which can be excluded due to the constraint $\mathbf{w}_k \cdot \hat{\mathbf{n}} = 0$ on $\partial\Omega \backslash \Sigma$.

Hence, in this discrete context, the solution is given by the vector field $\mathbf{j}(x,t) \in \underline{L_2(0,T) \otimes X}$ which satisfies (9)–(10) for any $\mathbf{w}(x) \in X$. Finally the problem takes the form

$$\mathbf{R}\mathbf{i} + \mathbf{L}\frac{\mathrm{d}}{\mathrm{d}t}\mathbf{i} + \mathbf{E}^T \boldsymbol{\phi} = \mathbf{v}^s \tag{37}$$

$$\mathbf{E}\mathbf{i} = \mathbf{i}^D \tag{38}$$

Here we introduced the resistance matrix $\mathbf{R}$, the inductance matrix $\mathbf{L}$ and the electrodes-currents *reduced* incidence matrix $\mathbf{E}$, besides the vectors of induced voltages due to external sources $\mathbf{v}^s$, which are defined as follows,

$$R_{jk} = \langle \eta \mathbf{w}_j, \mathbf{w}_k \rangle, j,\ k = 1, \ldots, N, \tag{39}$$

$$L_{jk} = \langle \mathcal{A} \mathbf{w}_j, \mathbf{w}_k \rangle, j,\ k = 1, \ldots, N. \tag{40}$$

$$(E)_{j,k} = \mathcal{I}_j \mathbf{w}_k = -\langle 1, \mathbf{w}_k \cdot \hat{\mathbf{n}} \rangle_{\Sigma_j} \quad \forall j = 1, \ldots, N_e - 1, \quad \forall k = 1, \ldots, N. \tag{41}$$

$$v_j^s = \langle -\partial \mathbf{a}_s / \partial t, \mathbf{w}_j \rangle \tag{42}$$

By definition the above matrices $\mathbf{R}$ and $\mathbf{L}$ are symmetric and positive definite. In particular the matrix $\mathbf{R}$ is positive definite if and only if the resistivity η is strictly positive, circumstance which we assume valid here. In the light of Remark 2.2, comparison of Eq. (38) with Eq. (10) suggests the interpretation of the matrix $\mathbf{E}$ as the reduced incidence matrix at the equipotential electrodes, hence constraining the unknown currents to the impressed ones $\mathbf{i}^D$.

Notice that the reduced incidence matrix $\mathbf{E}$ is the discrete version of the operator $\mathcal{I}$ introduced in Eq. (14). In particular in the kernel of $\mathbf{E}$ we will have all those vectors of X which do not determine current fluxes through the electrodes, *i.e.*

$$X_0 \equiv \ker(\mathbf{E}). \tag{43}$$

Clearly X_0 has dimension $N_0 = N - (N_e - 1)$. We collect the basis vectors for the null space of $\mathbf{E}$ as columns of the matrix $\mathbf{K} \in \mathbb{R}^N \times \mathbb{R}^{N_0}$. By simple linear algebra arguments, the orthogonal subspace X_D is generated by the image of $\mathbf{E}^T$:

$$X_D \equiv \mathrm{im}(\mathbf{E}^T). \tag{44}$$

which has dimension $N_e - 1$. Since X_D has the same dimensions as H_D, and linear combinations of vectors in X_D are sufficient to describe any admissible current flow across the electrodes Σ_k, it is clear that $X_D \equiv H_D$. The columns of $\mathbf{E}^T$ provide then a suitable set of basis vectors for H_D, as represented in the basis $\{\mathbf{w_k}, k = 1, \ldots, N\}$ of X. The discrete equivalent for the representation (16) is here given by

$$\mathbf{i} = \mathbf{K}\mathbf{i}_i + \mathbf{E}^T \mathbf{i}_e \tag{45}$$

The vector $\mathbf{I}_i \in L^2(0,T;\mathbb{R}^{N_0})$ represents the internal currents not crossing any electrode, while the vector $\mathbf{I}_e \in L^2(0,T,\mathbb{R}^{N_e-1})$ accounts for the current distributions impressed via the electrodes. Eq. (38) immediately reveals, since $\mathbf{E}$ is a full-rank matrix:

$$\mathbf{i}_e = (\mathbf{E}\,\mathbf{E}^T)^{-1}\mathbf{i}^D \ \rightarrow\ \mathbf{i} = \mathbf{K}\mathbf{i}_i + \mathbf{E}^T(\mathbf{E}\,\mathbf{E}^T)^{-1}\mathbf{i}^D. \tag{46}$$

Projecting Eq. (37) to the subspace X_0, which corresponds to left multiplication by $\mathbf{K}^T$, we find

$$\mathbf{R}_i \mathbf{i}_i + \mathbf{L}_i \frac{\mathrm{d}}{\mathrm{d}t}\mathbf{i}_i = -\mathbf{R}_{ie}\mathbf{I}_e - \mathbf{L}_{ie}\frac{\mathrm{d}}{\mathrm{d}t}\mathbf{i}_e + \mathbf{v}_{s,i}, \tag{47}$$

where

$$\mathbf{R}_i = \mathbf{K}^T \mathbf{R} \mathbf{K} \tag{48}$$

$$\mathbf{L}_i = \mathbf{K}^T \mathbf{L} \mathbf{K} \tag{49}$$

$$\mathbf{R}_{ie} = \mathbf{K}^T \mathbf{R} \mathbf{E}^T \tag{50}$$

$$\mathbf{L}_{ie} = \mathbf{K}^T \mathbf{L} \mathbf{E}^T \tag{51}$$

$$\mathbf{V}_{s,i} = \mathbf{K}^T \mathbf{V}_\mathbf{S} \tag{52}$$

The problem of finding $\mathbf{i} \in L^2(0,T;\mathbb{R}^N)$ satisfying Eqs. (37)–(38) has been reduced to the problem of finding $\mathbf{i}_i \in L^2(0,T,\mathbb{R}^{N_0})$ satisfying Eq. (47) following the same ideas and the same strategy which lead us to reduce the problem of finding $\mathbf{j}(x,t) \in H_L(\Omega,\Sigma)$ satisfying Eqs. (9)–(10) to the problem of finding $\mathbf{j}_0(x,t) \in H_0$ satisfying Eq. (20) in the exact framework.

The dynamical properties of the system are completely described by the resistance matrix $\mathbf{R}_i$ and the inductance matrix $\mathbf{L}_i$, which are both symmetric and positive definite. The matrices $\mathbf{L}_{ie}$ and $\mathbf{R}_{ie}$ account for the inductive and resistive coupling of the electrode-to-electrode currents $\mathbf{i}_e$ with the internal currents $\mathbf{i}_i$.

Remark 3.1. It is possible to plug Eq. (46) into the circuit Eq. (47) to make the current sources appear explicitly,

$$\mathbf{R}_i\mathbf{i}_i + \mathbf{L}_i\frac{\mathrm{d}}{\mathrm{d}t}\mathbf{i}_i = -\mathbf{R}_D\mathbf{i}^D - \mathbf{L}_D\frac{\mathrm{d}}{\mathrm{d}t}\mathbf{i}^D + \mathbf{v_i}^s, \tag{53}$$

where we defined

$$\mathbf{R}_D = \mathbf{R}_{ie}\left(\mathbf{E}\mathbf{E}^T\right)^{-1}, \tag{54}$$

$$\mathbf{L}_D = \mathbf{L}_{ie}\left(\mathbf{E}\mathbf{E}^T\right)^{-1}. \tag{55}$$

3.2. Modal decomposition

In this subsection, we introduce the discrete analog of the generalized eigenvalue problem (26). The next Section is devoted to illustrate how to use generalized eigenvalues and eigenvectors to accelerate time-domain eddy currents simulations.

Zeroing all the source terms in Eq. (53), we are left with the homogeneous problem

$$\mathbf{L}_i\frac{\mathrm{d}}{\mathrm{d}t}\mathbf{i}_i + \mathbf{R}_i\mathbf{i}_i = \mathbf{0}. \tag{56}$$

The problem of finding $\mathbf{I}_i(t) \in L^2(0,T;\mathbb{R}^{N_0})$ which satisfies (56) is the discrete analog of the problem of finding $\mathbf{j_0} \in L^2(0,T;H_0)$ which satisfies (22).

Both the inductance matrix $\mathbf{L}$ and $\mathbf{R}$ are real, symmetric and positive-definite. Indeed, $\mathbf{L}$ is the discrete equivalent of the symmetric and positive definite operator $\mathcal{A}$, whereas $\mathbf{R}$ is the discrete equivalent of the multiplication operator η, being an element of $L^\infty_+(\Omega)$. These properties hold also for $\mathbf{L}_i = \mathbf{K}^T\mathbf{L}\mathbf{K}$ and $\mathbf{R}_i = \mathbf{K}^T\mathbf{R}\mathbf{K}$, because $\mathbf{K}$ is a full rank matrix.

Since both $\mathbf{L}_i$ and $\mathbf{R}_i$ are real, symmetric matrices and positive-definite matrices, the generalized eigenvalue problem [26]

$$\mathbf{L}_i\mathbf{v} = \tau\mathbf{R}_i\mathbf{v} \tag{57}$$

admits a basis $\{\mathbf{v}_1,\dots,\mathbf{v}_{N_0}\}$ of generalized eigenvectors and associated real positive eigenvalues $\{\tau_1,\dots,\tau_{N_0}\}$. The eigenvectors are orthogonal with respect to the scalar products induced both by the inductance and the resistance matrix, i.e.

$$\mathbf{v}_k^T\,\mathbf{L}_i\,\mathbf{v}_j = \begin{cases} 0 & \forall k \neq j \\ l_k & k = j \end{cases}, \tag{58}$$

$$\mathbf{v}_k^T\,\mathbf{R}_i\,\mathbf{v}_j = \begin{cases} 0 & \forall k \neq j \\ r_k & k = j \end{cases}, \tag{59}$$

where $\tau_i = l_i/r_i$. The monotonicity principle [22] still holds in the discrete finite context. In addition, re-scaling the resistance matrix $\mathbf{R}$ by some multiplicative factor k the eigenvectors are preserved and the eigenvalues are re-scaled by a factor k^{-1}. Further, it is possible to order the eigenvalues, corresponding to the time constants of the different eigenmodes, in decreasing order. Given this choice, and thanks to the properties of modes and eigenvalues introduced in the continuum context in previous Section, it follows that the smallest eigenvalue approaches asymptotically zero. In practice we have to construct a finite approximation of $H_L(\Omega,\Sigma)$ such that the smallest time constant is sufficiently lower than time scale of the fastest dynamics we are interested in. Moreover the following characterization of the eigenvalues holds [27]:

$$\tau_n = \max_{\dim U = n}\min_{\mathbf{x}\in U}\frac{\mathbf{x}^T\,\mathbf{L}_i\,\mathbf{x}}{\mathbf{x}^T\,\mathbf{R}_i\,\mathbf{x}} \tag{60}$$

The original coupled system of first-order Ordinary Differential Eq. (53) is decoupled into N_0 non-interacting ODEs when moving to the basis of generalized eigenvectors:

$$l_n\tilde{i}'_n + r_n\tilde{i}_n = \tilde{e}_n, \forall n = 1,\dots,N_0. \tag{61}$$

In Eq. (61) $l_n = \mathbf{v}_n^T\,\mathbf{L}_i\,\mathbf{v}_n$, $r_n = \mathbf{v}_n^T\,\mathbf{R}_i\,\mathbf{v}_n$ and the forcing term is $\tilde{\mathbf{e}}_n = -\mathbf{v}_n^T(\mathbf{L}_D d\mathbf{i}^D/dt + \mathbf{R}_D\mathbf{i}^D + \mathbf{v}_i^s)$. The time constant associated to the nth eigenmode is clearly given by the associated eigenvalue $\tau_n = l_n/r_n$. We can advance separately in time each eigenmode of the dynamical system, providing the engineer with several possible exact or approximate methods for the fast time integration of the system.

3.3. Time integration scheme

The modal decomposition of the dynamical system opens a new range of opportunities for the time integration of the dynamical system, since analytical solutions to polynomial input signals become now easily manageable. We postpone the exploration of analytical and semi-analytical techniques to future work on the subject, while here we explore the computational advantages obtained via modal decomposition even in the framework of the same time integration technique.

3.3.1. Cholesky decomposition

The standard approach to find the solution $\mathbf{I}_i(t) \in L^2(0,T;\mathbb{R}^{N_0})$ of the discrete eddy current problem (53) is to use a θ-method, so to allow eventually for larger time steps:

$$\begin{aligned}\left(\mathbf{L}_i + \Delta t\,\theta\,\mathbf{R}_i\right)\delta\mathbf{i}_i^{(k+1)} = &-\Delta t\mathbf{R}_i\,\mathbf{i}_i^{(k)} - \Delta t\mathbf{R}_D\,\mathbf{i}^{D,(k)} \\ &- \left(\mathbf{L}_D + \Delta t\,\theta\,\mathbf{R}_D\right)\delta\mathbf{i}^{D,(k+1)} + \Delta t\left[(1-\theta)\mathbf{v}_i^{s(k)} + \theta\mathbf{v}_i^{s(k+1)}\right]\end{aligned} \tag{62}$$

where

$$\begin{aligned}\delta\mathbf{i}_i^{(k+1)} &= \left(\mathbf{i}^{(k+1)} - \mathbf{i}^{(k)}\right),\\ \delta\mathbf{i}_i^{D,(k+1)} &= \left(\mathbf{i}^{D,(k+1)} - \mathbf{i}^{D,(k)}\right).\end{aligned} \tag{63}$$

Here θ is a numerical parameter to choose in the interval $[0,1]$, the implicit Euler scheme corresponding to the case $\theta = 1$. Since the matrix $\mathbf{Z} = \left(\mathbf{L}_i + \Delta t\,\theta\mathbf{R}_i\right)$ is symmetric and positive definite, a convenient method to solve (62) is based on the Cholesky decomposition. For fixed time integration scheme (*i.e.* fixed θ parameter), and for fixed time step Δt, we can compute the Cholesky decomposition of $\mathbf{Z}$ once for all, *i.e.* $\mathbf{Z} = \mathbf{C}\,\mathbf{C}^T$, where $\mathbf{C}$ is a real lower triangular matrix. At each time step we just need to solve the lower triangular problem $\mathbf{C}\,\mathbf{y} = \mathbf{b}$ (forward substitution) and the upper triangular problem $\mathbf{C}^T\,\delta\mathbf{i}_i^{(k+1)} = \mathbf{y}$ (backward substitution). We defined with the symbol $\mathbf{b}$ the right hand side of the linear algebraic system, depending solely by the currents at the previous time step $\mathbf{i}_i^{(k)}$ and by the forcing terms.

The overall computational cost of a simulation will be proportional to the cost of computing the Cholesky decomposition for the dynamic matrix $\mathbf{Z}$, plus the cost of the backward and forward substitutions at each time step.

Once the discrete samples $\mathbf{i}_i^{(k)}$s of the solution have been evaluated, consecutive values can be linearly interpolated to find the solution $\mathbf{I}_i(t)$ for any $t \in (0,T)$.

3.3.2. Modal decomposition

Applying the θ-method described in previous section to the set of N_0 linearly independent Eq. (61), we find

$$\left(l_n + \Delta t\,\theta\,r_n\right)\delta\tilde{i}_n = -\Delta t\,r_n\tilde{i}_n^{(k)} + \theta\tilde{e}_n^{(k+1)} + (1-\theta)\tilde{e}_n^{(k)}, \tag{64}$$

which is immediate to invert. The overall computational cost of a simulation will be proportional to the cost of computing the generalized eigenvalues and eigenvectors, performing necessary projections (see definition of $\tilde{\mathbf{e}}_n$ below Eq. (61)), plus the cost of solving N independent linear scalar equations at each time step.

With respect to the forcing term $\tilde{e}_n$ defined in (61), it should be noted that it can be computed in a very efficient way. Indeed, the multiplications $-\mathbf{v}_n^T\mathbf{L}_D$ and $-\mathbf{v}_n^T\mathbf{R}_D$ can be computed once for all, and, since $N_e \ll N_0$, the computational cost of this multiplication is almost linear in the number of unknowns. Furthermore, in practical applications, the geometry of the source currents is fixed. This is the case, for example, of a coil generating a magnetic field coupling with the conductors. This guarantees that the source current density $\mathbf{j}_S(x,t)$ admits a factorization of the form $\mathbf{j}_S(x,t) = \alpha(t)\mathbf{u}_s(x)$ and, as a consequence, $\mathbf{v}_i^s = \alpha(t)\widetilde{\mathbf{v}}_i^s$, where $\widetilde{\mathbf{v}}_s^i$ depends only on the geometry of the excitation, while $\alpha(t)$ accounts for the time-behavior of the source current density. Thus, also in this case, the product $-\mathbf{v}_n^T\widetilde{\mathbf{v}}_i^s$ has to be computed once for all. In other words, the updating in (64) requires only the multiplication for $\alpha(t)$.

Moreover, thanks to the decoupling between the equations, it is also possible to choose the time step Δt and/or the integration scheme independently for each equation, thus improving the overall computational costs.

4. Results

In this last section, the performances of the proposed method are evaluated on a practical problem in the framework of Nondestructive Testing (NdT) based on eddy currents.

Eddy currents can be effectively exploited to detect and retrieve useful information about defects in metallic samples. Indeed, the presence of flaws produces a perturbation in the eddy current circulation, resulting in a peculiar reaction magnetic flux density. In this context, numerical simulations play a paramount role, being an essential tool in designing and optimizing the equipment required in the overall inspection process.

However, the computational time required by such kind of numerical simulations is very relevant and, hence, there is a strong demand of new numerical techniques able to accelerate the process. In Section 4.7, it is shown that the proposed method is able to drastically reduce the computational time with respect to the already available methods.

4.1. The NdT problem

The NdT problem of interest is the inspection of metallic pipelines for the transportation of oil and natural gas (see Section 1 and ref.[11]), from the exterior of the pipe (NoPig methods). Although the use of pigs, i.e. proper probes inserted in the interior of the pipe, is a well-established method for monitoring the state of the walls of pipelines, there is a strong demand for methodologies that do not require their use. Indeed, there are multiple cases where it is not possible to access to the interior of the pipe or there is the need of measuring relatively far from the tube [12].

In NoPig methods, the excitation is given by alternating currents directly injected into the pipeline walls and magnetic sensors are employed to measure the magnetic field around the tube [11,15]. Generally, measurements at multiple frequencies are required for the detection of flaws at different depths, in a range from some Hz to hundreds of kHz.

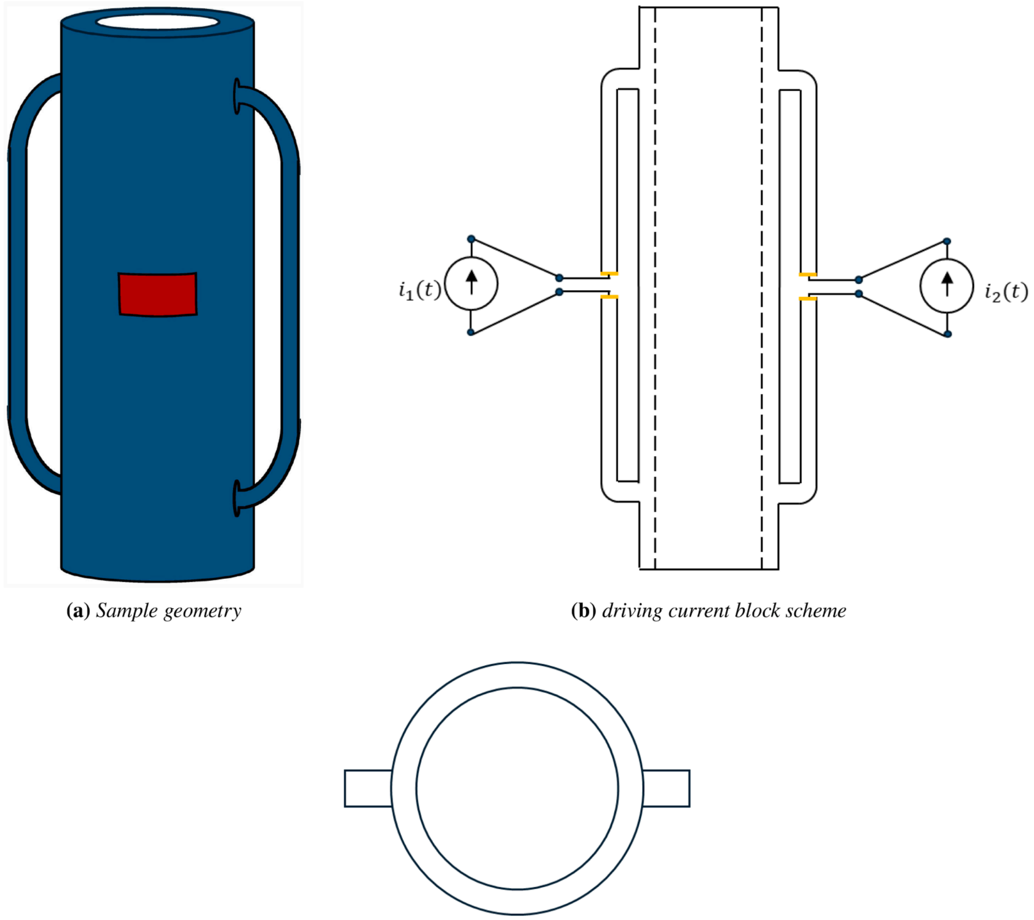

(a) *Sample geometry*

(b) *driving current block scheme*

(c) *tube cross section*

Fig. 4. (a) Geometry of the sample, in red the position of the analyzed cracks. (b) Longitudinal cross-section of the tube. The driving current is injected throughout two pairs of electrodes (marked in yellow). (c) Transverse cross-section of the tube. (For interpretation of the references to colour in this figure legend, the reader is referred to the web version of this article.)

In order to reduce the measurement time, multi-sine signals are employed [28], which give the opportunity to collect the data from all the frequency of interest simultaneously. On the other hand, the numerical simulation of this problem, given this kind of driving current, can be particularly challenging, since both small time steps and long time simulations are required.

In this paper, the sample under test is a commercial cylindrical tube with an outer diameter of 168.28 mm, a thickness of 3 mm and a length of 1.5 m. The excitation is given by alternating currents injected through two diametrically opposite pairs of conductive legs at the ends of the tube (see Fig. 4). The electrical resistivity is $\eta = 1.09 \times 10^{-6}\,\Omega \cdot m$, which is the one of a particular aluminum alloy (Inconel 600), a material widely used in a range of applications.

In the following, it is shown that the present numerical methodology can be successfully applied to compute accurately and efficiently the magnetic response from different flaws. This is a mandatory step in almost every method for the solution of the inverse problem, i.e. to retrieve the presence, position and size of the flaws, starting from the measured data.

First, the response of a defect-free sample, in terms of magnetic flux density, is simulated and used as reference. Subsequently, the responses from configurations with different representative defects are compared with the reference (defect-free sample) at several driving frequencies. For a detailed description of the data processing see Section 4.5.

4.2. Defects definition

Three different configurations are analyzed: a defect-free configuration used as reference (background signal), a tube with a surface breaking crack situated in the outermost position and a configuration with a buried crack located in the innermost tube position. Fig. 5 shows the details of the two cracks.

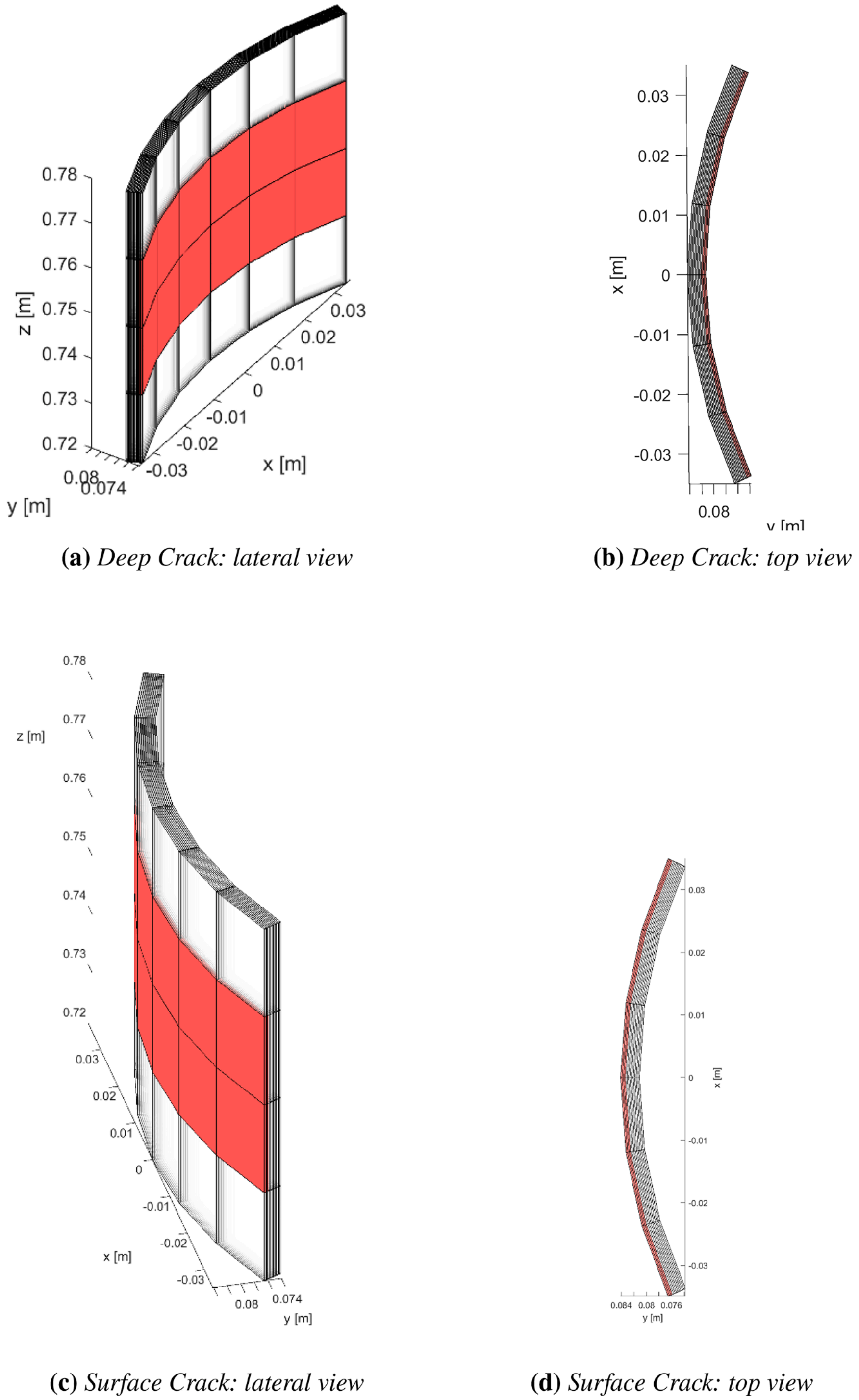

(a) *Deep Crack: lateral view*

(b) *Deep Crack: top view*

(c) *Surface Crack: lateral view*

(d) *Surface Crack: top view*

Fig. 5. Geometry of the simulated cracks.

The different location of the cracks is required to assess the performances of the eddy-currents testing system across the range of selected frequencies. Indeed, by a physical standpoint, the inner cracks react only to lower frequencies, due to the penetration depth of the magnetic field, while surface cracks can be revealed by both lower and higher frequencies, but with different kinds of magnetic response.

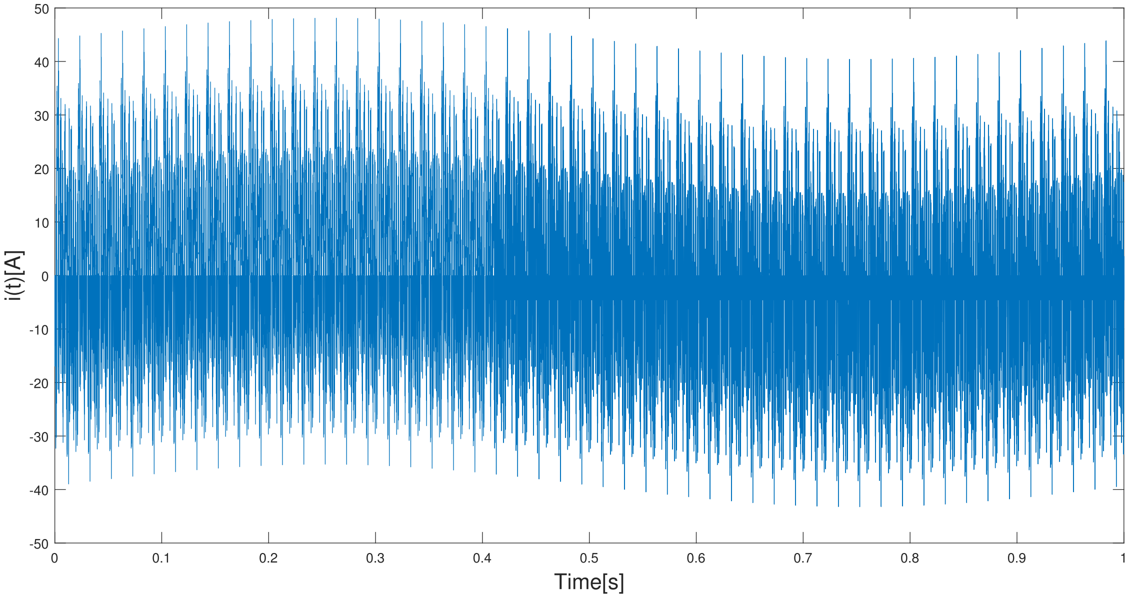

Fig. 6. Waveform of the driving current. The current has a quite constant envelope, with a maximum value of about 48 A and a minimum value of about −43 A.

4.3. Driving current

In order to retrieve data from the cracks at different frequencies, a multi-sine waveform is adopted as driving current

$$i(t) = \sum_{k=1}^{N_s} I_k \sin\left(2\pi f_k t + \phi_k\right). \tag{65}$$

Such signals are commonly used in eddy current testing, since they can significantly reduce measurement time in practical applications, giving the opportunity to collect information from various frequencies in only one measurement step [28]. On the other hand, this driving current poses serious challenges from a computational point of view. Indeed, a proper time-domain simulation of the sample response requires long simulation times (due to tones at lower frequencies) and small time steps (due to tones at higher frequencies).

For the case of interest, $N_s = 30$ tones with equal amplitude $I_k = 4$ A are adopted. The tone frequencies are {1, 50, 100, 150, 250, 300, 400, 600, 700, 800, 900, 1000, 1500, 2000, 2500, 3000, 3500, 4000, 4500, 5000, 5500, 6000, 6500, 7000, 7500, 8000, 8500, 9000, 9500, 10000} Hz and they are selected such that the penetration depth varies in a range compatible with the thickness of the tube. The phases ϕ_k are chosen in order to avoid a large peak to the RMS ratio of $i(t)$. As described in [28], an optimal choice is

$$\phi_k = -\pi \frac{k(k-1)}{N_s},$$

which ensures that $i(t)$ has a quite constant envelope, a fundamental requirement to optimize the range of the analog to digital converter in acquisition. The obtained driving signal is depicted in Fig. 6.

4.4. Sensing points

In order to characterize the response of the two analyzed cracks, the values of the magnetic flux density are collected from $N_p = 301$ points placed around the tube, simulating the measurements made by an array of magnetic sensors. Specifically, the points are distributed at a fixed distance of 3 mm from the tube, a fixed height of 750 mm from the bottom of the tube and they span π radians around the defect (see Fig. 7).

4.5. Crack signature

The data collected from the sensing points are subsequently processed to obtain useful information about the cracks. The purpose is to characterize the different cracks through an appropriate figure of merit capable of providing a representation of the peculiar characteristics of each. Such figure is the so-called *crack signature*, and allows to evaluate the distinctive response of a given crack with respect to the measurement points, at a prescribed driving frequency. Assuming the $e^{j\omega_k t}$ time behaviour, with $\omega_k = 2\pi f_k$, the *crack signature*, for the two crack analyzed, is defined as

$$\Delta\mathbf{B}_k^{ci}(\varphi_h) = \mathbf{B}_k^{ci}(\varphi_h) - \mathbf{B}_k^{bg}(\varphi_h) \tag{66}$$

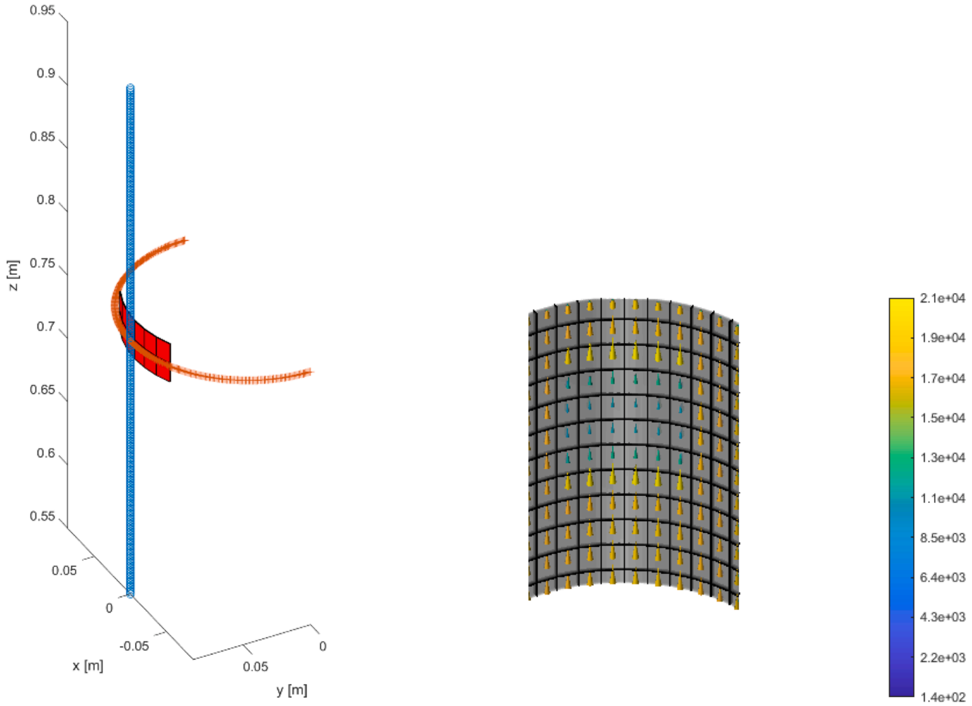

(a) *Sensing points*	**(b)** *Perturbation by flaws*

Fig. 7. (a) position of sensing points. (b) zoom of the current density perturbation due to the crack.

$$\Delta \mathbf{B}_k^{co}(\varphi_h) = \mathbf{B}_k^{co}(\varphi_h) - \mathbf{B}_k^{bg}(\varphi_h), \tag{67}$$

where $\mathbf{B}_k(\varphi_h)$ is the phasor related to the φ-component of the magnetic flux density at the frequency f_k and in the measurement point described by the angular coordinate φ_h. The superscripts refer to the background configuration (bg), to the configuration with the inner crack (ic) and to the configuration with the outer crack (oc), respectively.

From the *crack signature*, it is possible to infer some useful information about cracks shape and position. For example, the signals produced by the surface crack have an higher amplitude for higher frequencies even if it can be detected by means of lower frequencies also. On the other hand, useful information on the inner crack can be obtained by using lower frequencies only, due to the penetration depth. For the cracks analyzed in this paper, similar considerations can be drawn from Fig. 8, where the behaviour of $\Delta\mathbf{B}_1^{ci}$, $\Delta\mathbf{B}_1^{co}$ and $\Delta\mathbf{B}_{30}^{ci}$, $\Delta\mathbf{B}_{30}^{co}$ with respect to the sensing points is depicted in the complex plane.

As a final remark, we highlight that the analysis of the crack signature, is a standard *tool* in Eddy Current Testing. For example, in [29–31] are described some methods able to retrieve information about the length of defects as well as their orientation, starting from the crack signature. In addition, in [30], the central role of numerical simulations is highlighted, where numerical data are exploited to build a database of crack signature related to prescribed crack geometries. In turn, this database can be exploited as a *component* in inversion method.

4.6. Numerical approaches

As underlined in the previous section, the outcome of the computation is the magnetic flux density $\Delta\mathbf{B}_k$, evaluated at the N_s frequencies of interest.

From a numerical point of view, the *crack signature* can be evaluated by two different approaches:

- methods in the frequency domain (FD);
- methods in the time domain (TD).

In frequency-domain approaches, problem (9), (10) is solved repeatedly at each individual harmonic driving current $i(t) = I_k \sin(2\pi f_k t)$, where $\omega_k = 2\pi f_k$ is the k−th angular frequency. In this case the solution of N_s different problems is needed. If a direct method is used to solve such problems, then this techniques requires N_s factorizations of dense matrices.

In time-domain approaches, the solver computes the solution of problem (9), (10) for the input current of (65). For the case of interest, a sampling rate of 30,000 samples per second is chosen ($f_{30} = 10\,\text{kHz}$). Then, the phasors of interest can be computed

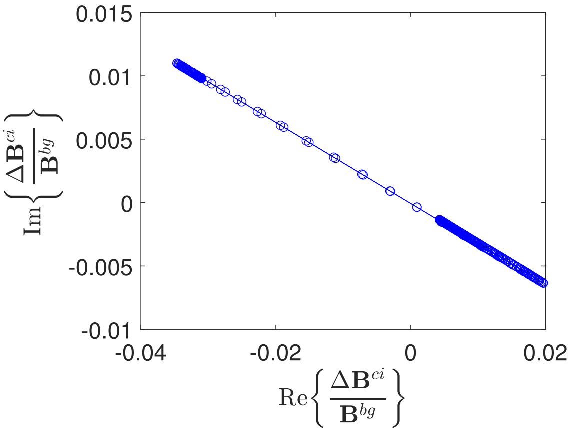

(a) *Normalized* $\Delta\mathbf{B}_1^{ci}$, $f_1 = 1\,Hz$

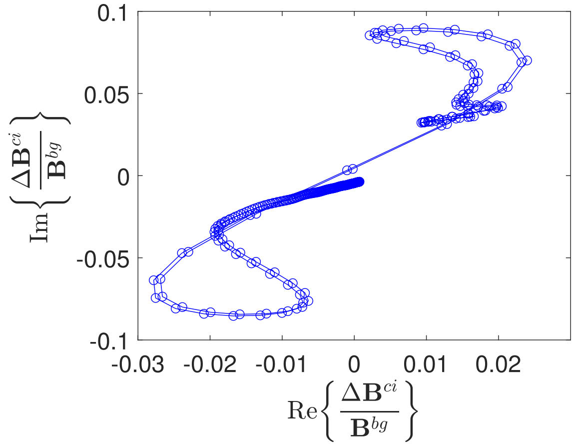

(b) *Normalized* $\Delta\mathbf{B}_{30}^{ci}$, $f_{30} = 10\,kHz$

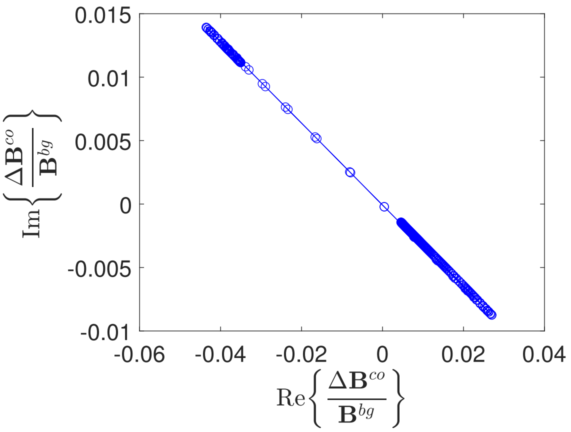

(c) *Normalized* $\Delta\mathbf{B}_1^{co}$, $f_1 = 1\,Hz$

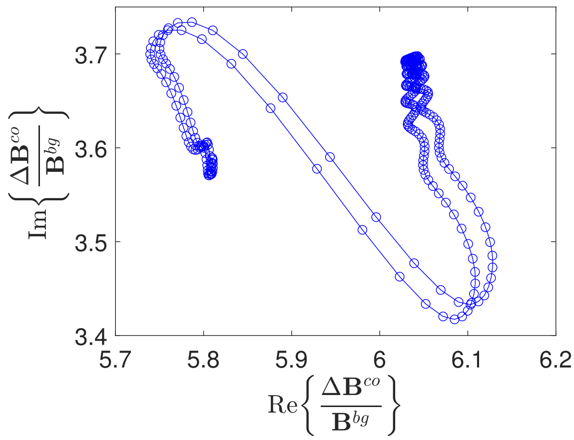

(d) *Normalized* $\Delta\mathbf{B}_{30}^{co}$, $f_{30} = 10\,kHz$

Fig. 8. Characterization of the defect response. Top: outer defect, bottom: inner defect.

via a Fast Fourier Transform. The outcome of the numerical simulations are $B_\varphi^{bg}(\varphi,t)$, $B_\varphi^{ci}(\varphi,t)$ and $B_\varphi^{co}(\varphi,t)$, where φ is the angular coordinate in the standard cylindrical coordinates, B_φ stands for the φ-component of the magnetic flux density field. These data are processed as follows

1. Compute the phasors $\{\mathbf{B}_k^{bg}(\varphi_h)\}_{h,k}$, $\{\mathbf{B}_k^{ci}(\varphi_h)\}_{h,k}$, $\{\mathbf{B}_k^{co}(\varphi_h)\}_{h,k}$ related to $B_\varphi^{bg}(\varphi,t)$, $B_\varphi^{ci}(\varphi,t)$ and $B_\varphi^{co}(\varphi,t)$, via Fast Fourier Transform.
2. Compute the *crack signatures* as defined in (66), (67).

In the time-domain framework, two different techniques are investigated

- the proposed method based on mode expansion of the field (TD1).
- traditional integration scheme based on Cholesky factorization (TD2);

The numerical examples are carried out by means of in-house software implementing the three methods considered in the comparison. The software is based on the Finite Elements Method and implements parallel computing. Linear algebra computations are based on the usage of SCALAPACK library and, in particular, PDSYGVX for the solution of the generalized eigenvalue problem (TD1 approach), PDPOTRF is used for the factorization of real matrices (TD2 approach), and PZGETRF for the factorization of complex matrices (FD approach).

The mesh employed in domain's discretization has 58332 nodes and 52940 hexahedral elements, with a total of 100676 degrees of freedom (see Fig. 9).

4.7. Computational cost

The computations described in the previous sections are executed twice in the time-domain, with the proposed approach and with a standard integration scheme based on Cholesky factorization, and in the frequency domain also. The resulting simulation times are reported in Table 2.

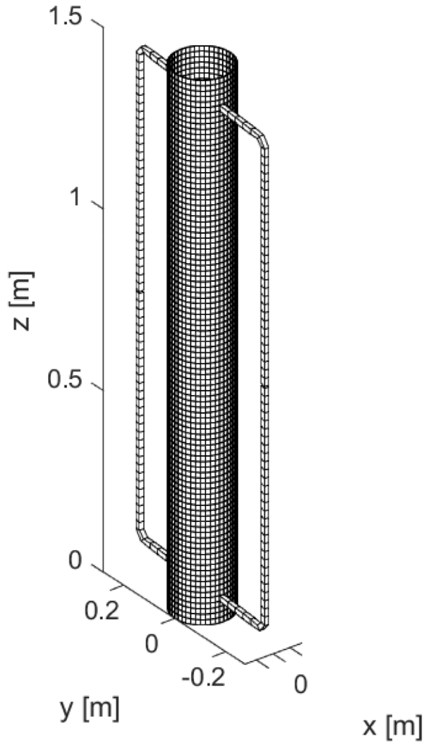

Fig. 9. Finite element discretization used in the numerical model.

Table 2
Computational time comparison between the proposed approach (TD1), a traditional integration scheme (TD2) and the solution in the frequency domain (FD).

Method	Setup Time (h)	Processing (h)	Total (h)
TD1	~ 8	~ 12	~ 20
TD2	0.5	~ 70	~ 71
FD	~ 40	~ 0.04	~ 40

The computational time has been divided into Setup and Processing, according to the following classification

- Setup Time
  - Proposed approach (TD1): solution of the generalized eigenvalue problem (57).
  - Traditional integration scheme (TD2): computation of the Cholesky decomposition of $\mathbf{L}_i + \Delta t\,\theta\,\mathbf{R}_i$.
  - Solution in the frequency domain (FD): computation of N_s factorizations, one for each frequency.
- Processing Time
  - Proposed approach (TD1): solution of (64) at each time step, given the generalized eigenvalues/ eigenvectors.
  - Traditional integration scheme (TD2): solution of (62) via backward and forward substitutions at each time step, given the factorization of $\mathbf{L}_i + \Delta t\,\theta\,\mathbf{R}_i$.
  - Solution in the frequency domain (FD): solution of the resulting N_s linear systems via backward and forward substitution.

The time spent in assembling the matrix $\mathbf{L}_i + \Delta t\,\theta\,\mathbf{R}_i$ or the equivalent matrices for frequency-domain approach has been neglected since much lower of the factorization time.

The results presented in Table 2 are achieved utilizing 49 MPI processes on a shared-memory machine. This machine is equipped with dual AMD Epyc 32-Core 7452 processors and boasts 1 TB of RAM.

As it can be seen, the proposed approach allows to obtain a relevant gain (about 3.5x) on the total computational time, reducing it from 3 days to 20 h roughly, with respect to the traditional integration scheme in the time domain. The gain is achieved by a significant decrease of the time needed for the solution of the transient problem, even if the setup time required is much higher with respect to the Cholesky decomposition. Furthermore, the method performs well with respect to the solution in the frequency domain, where the gain is roughly of 2x.

Summing up, the proposed approach outperforms traditional methods when the simulation for a large number of time steps is required, or the simulation for a large number of different frequencies is required. Moreover, the longer set-up time is largely compensated when several time domain simulations with the same geometry but different driving terms, and/or different time steps, are required.

5. Conclusions

In this contribution we illustrated the use of a modal decomposition approach for the simulation of large time-domain eddy current problems, in presence of injected currents in the conductors through equipotential electrodes. In this respect, we illustrated how to apply the approach of [22], where the modal decomposition was introduced for the eddy current problem in the absence of boundary electrodes, to the case where impressed currents are present. The key ingredient to get the modal decomposition for this more general case is the identification of two orthogonal subspaces generating $H_L(\Omega, \Sigma)$ as a direct sum. In particular it can be proved that $H_L(\Omega, \Sigma) = H_0 \oplus H_D$, where H_0 contains current densities $\mathbf{u}$ related to vanishing net electrical currents through each electrode $\left(\langle 1, \mathbf{j} \cdot \hat{\mathbf{n}} \rangle_{\Sigma_k} = 0,\ k = 1, \dots, N_e\right)$ whereas H_D represent current densities with net electrical currents entering two or more electrodes. Moreover, we proved that H_D is $(N_e - 1)$-dimensional, where N_e is the number of boundary electrodes.

The numerical method following the modal decomposition has been designed to be very effective in the context of direct methods, where the linear system of interest is solved by means of a direct method. Using direct methods is feasible as long as the size of the stiffness matrix of the underlying eddy current problem does not exceed a threshold value depending on the computer hardware. In these cases, the computation of the *complete* set of modes requires a computational cost in the range of that of direct methods. For larger problems, iterative methods are mandatory and, moreover, the computation of the complete set is expensive, and strategies for selecting and computing only the dominant modes are essential.

The efficiency of the proposed approach was clearly demonstrated for a Non-destructive-Testing application. In particular we considered an Inconel 600 pipe, and simulated the crack signature of two possible pipe defects both via the proposed modal decomposition and via the usual Cholesky factorization. In terms of pre-computation, the evaluation of the generalized eigenvectors and eigenvalues requires more time than that for the Cholesky factorization of the dynamical matrix ($\simeq 8$ h and 0.5 h, respectively). Nevertheless, both computational times scale with the same law: $C_{CF} N^3$ for the Cholesky factorization and $C_{GEP} N^3$ for computing the Generalized Eigenvalue Problem, where C_{CF} and C_{GEP} are proper constants. On the other hand, the computational cost required at each individual time step scales as $C_{TS} N$ for the modal decomposition, and as $C_{BS} N^2$ for the backsubstitutions following the Cholesky factorization of the dynamical matrix. Both C_{TS} and C_{BS} are proper constants.

In our NDT test case, a driving multisine signal made by the superposition of sinusoidal tones from a wide frequency range was necessary to identify the crack features. Hence, it was necessary to set up a relatively long simulation interval, resulting in a large number of time steps. This circumstance determined an overall advantage in using the modal decomposition approach compared to the standard one. NDT physicists and engineers which need to perform long eddy currents time-domain simulations with a relatively small time step, can definitely benefit of the modal decomposition approach proposed in this contribution. This advantage is even more evident when different simulations of the same geometry at different time steps need to be performed: the generalized eigenmode analysis is independent from the chosen time step, and the inversion of a diagonal matrix requires only N operations. On the other hand the matrices resulting from the Cholesky factorization depend on the time step, and the factorization has to be repeated any time one wants to change the time step of the simulation.

CRediT authorship contribution statement

Salvatore Ventre: Writing – review & editing, Software, Data curation, Conceptualization; **Vincenzo Mottola:** Writing – review & editing, Writing – original draft, Validation, Software, Methodology, Investigation, Data curation; **Nicola Isernia:** Writing – review & editing, Writing – original draft, Software, Formal analysis, Conceptualization; **Andrea Gaetano Chiariello:** Writing – review & editing, Writing – original draft, Validation, Software, Conceptualization; **Antonello Tamburrino:** Writing – review & editing, Writing – original draft, Supervision, Software, Funding acquisition, Formal analysis, Data curation, Conceptualization.

Financial disclosure

None reported.

Data availability

Data will be made available on request.

Declaration of competing interest

The authors declare the following financial interests/personal relationships which may be considered as potential competing interests: Antonello tamburrino reports financial support was provided by Italian Ministry of University and Research. If there are other authors, they declare that they have no known competing financial interests or personal relationships that could have appeared to influence the work reported in this paper.

Acknowledgment

This work has been partially supported by the Italian Ministry of University and Research (Project no. 2022Y53F3X, PRIN 2022). Some of the work leading to this manuscript was performed using the Marconi-Fusion supercomputer operated by CINECA, through the EUROfusion HPC project “Generalized Eigenvalues Methods for Modeling Plasma Fusion Devices.”

References

[1] R. Albanese, G. Rubinacci, Integral formulation for 3D eddy-current computation using edge elements, IEE Proc. A Phys. Sci. Meas. Instrum. Manage. Educ. Rev. 135 (7) (1988) 457. https://doi.org/10.1049/ip-a-1.1988.0072

[2] R. Albanese, G. Rubinacci, Finite Element Methods for the Solution of 3D Eddy Current Problems, 102 of Advances in Imaging and Electron Physics, Elsevier, (1997), pp. 1–86. https://doi.org/10.1016/S1076-5670(08)70121-6

[3] M. Passarotto, S. Pitassi, R. Specogna, Foundations of volume integral methods for eddy current problems, Comput. Methods Appl. Mech. Eng. 392 (2022) 114626. https://doi.org/10.1016/j.cma.2022.114626

[4] G. Rubinacci, A. Tamburrino, F. Villone, Circuits/fields coupling and multiply connected domains in integral formulations, IEEE Trans. Magn. 38 (2) (2002) 581–584. https://doi.org/10.1109/20.996152

[5] P. Bettini, N. Marconato, M.F. Palumbo, S. Peruzzo, R. Specogna, R. Albanese, G. Rubinacci, S. Ventre, F. Villone, Numerical modeling of 3D halo current path in ITER structures, Fusion Eng. Des. 88 (6-8) (2013) 529–532. https://doi.org/10.1016/j.fusengdes.2012.11.017

[6] C.-C. Tai, J.H. Rose, J.C. Moulder, Thickness and Conductivity of Metallic Layers from Pulsed Eddy Current Measurements, Springer US, Boston, MA, (1996), pp. 409–416. https://doi.org/10.1007/978-1-4613-0383-1_52

[7] W. Cheng, I. Komura, Simulation of transient eddy-current measurement for the characterization of depth and conductivity of a conductive plate, IEEE Trans. Magn. 44 (11) (2008) 3281–3284. https://doi.org/10.1109/TMAG.2008.2001613

[8] Z. Su, S. Ventre, L. Udpa, A. Tamburrino, Monotonicity based imaging method for time-domain eddy current problems, Inverse Probl. 33 (12) (2017) 125007. https://doi.org/10.1088/1361-6420/aa909a

[9] J. Vrana, R. Singh, NDE 4.0—a design thinking perspective, J. Nondestr. Eval. 40 (2021). https://doi.org/10.1007/s10921-020-00735-9

[10] R. Jarvis, P. Cawley, P.B. Nagy, Current deflection NDE for the inspection and monitoring of pipes, NDT E Int. 81 (2016) 46–59. https://doi.org/10.1016/j.ndteint.2016.03.006

[11] R. Jarvis, P. Cawley, P.B. Nagy, Performance evaluation of a magnetic field measurement NDE technique using a model assisted probability of detection framework, NDT E Int. 91 (2017) 61–70. https://doi.org/10.1016/j.ndteint.2017.06.006

[12] G.S. Krivoi, NoPig: an above-ground inspection technique for non-piggable pipelines, Oil Gas Eur. Mag. 34 (2008) 122–124.

[13] J. Bowler, N. Bowler, Theory of four-point alternating current potential drop measurements on conductive plates, Proc. R. Soc. A Math. Phys. Eng. Sci. 463 (2007). https://doi.org/10.1098/rspa.2006.1791

[14] H. Saguy, D. Rittel, Alternating current flow in internally flawed conductors: a tomographic analysis, Appl. Phys. Lett. 89 (2006). https://doi.org/10.1063/1.2338655

[15] M.S.H. Leung, J. Corcoran, P.B. Nagy, The influence of the dynamic magnetoelastic effect on potential drop measurements, NDT E Int. 102 (2019) 153–160. https://doi.org/10.1016/j.ndteint.2018.11.014

[16] A. Saxena, Electrical potential technique for monitoring subcritical crack growth at elevated temperatures, Eng. Fract. Mech. 13 (4) (1980) 741–750. https://doi.org/10.1016/0013-7944(80)90005-3

[17] J. Corcoran, P. Hooper, C. Davies, P.B. Nagy, P. Cawley, Creep strain measurement using a potential drop technique, Int. J. Mech. Sci. 110 (2016) 190–200. https://doi.org/10.1016/j.ijmecsci.2016.03.015

[18] J. Corcoran, P. Nagy, Magnetic stress monitoring using a directional potential drop technique, J. Nondestr. Eval. 37 (2018). https://doi.org/10.1007/s10921-018-0510-4

[19] J.R. Bowler, Y. Huang, H. Sun, J. Brown, N. Bowler, Alternating current potential-drop measurement of the depth of case hardening in steel rods, Meas. Sci. Technol. 19 (7) (2008) 075204. https://doi.org/10.1088/0957-0233/19/7/075204

[20] M. Hölzl, P. Merkel, G.T.A. Huysmans, E. Nardon, E. Strumberger, R. McAdams, I. Chapman, S. Günter, K. Lackner, Coupling JOREK and STARWALL codes for non-linear resistive-wall simulations, J. Phys. Conf. Ser. 401 (1) (2012) 012010. https://doi.org/10.1088/1742-6596/401/1/012010

[21] N. Isernia, N. Schwarz, F.J. Artola, S. Ventre, M. Hoelzl, G. Rubinacci, F. Villone, J. Team, Self-consistent coupling of JOREK and CARIDDI: on the electromagnetic interaction of 3D tokamak plasmas with 3D volumetric conductors, Phys. Plasmas 30 (11) (2023) 113901. https://doi.org/10.1063/5.0167271

[22] A. Tamburrino, G. Piscitelli, Z. Zhou, The monotonicity principle for magnetic induction tomography, Inverse Probl. 37 (9) (2021) 095003.

[23] A. Bossavit, Computational Electromagnetism: Variational Formulations, Complementarity, Edge Elements, Academic Press, (1998).

[24] A. Bossavit, On the numerical analysis of eddy-current problems, Comput. Methods Appl. Mech. Eng. 27 (3) (1981) 303–318.

[25] H.A. Haus, J.R. Melcher, Electromagnetic Fields and Energy, 107, Prentice Hall Englewood Cliffs, NJ, (1989).

[26] Y. Saad, Numerical Methods for Large Eigenvalue Problems, Society for Industrial and Applied Mathematics, (2011). https://doi.org/10.1137/1.9781611970739

[27] Z. Su, S. Ventre, L. Udpa, A. Tamburrino, Monotonicity based imaging method for time-domain eddy current problems*, Inverse Probl. 33 (12) (2017) 125007. https://doi.org/10.1088/1361-6420/aa909a

[28] A. Sardellitti, G.D. Capua, M. Laracca, A. Tamburrino, S. Ventre, L. Ferrigno, A fast ECT measurement method for the thickness of metallic plates, IEEE Trans. Instrum. Meas. 71 (2022) 1–12. https://doi.org/10.1109/TIM.2022.3188029

[29] D. Pasadas, A.L. Ribeiro, H. Ramos, Analysis of the magnetic field in the presence of linear sub-surface cracks using ECT, Acta IMEKO 7 (1) (2018) 36–41.

[30] F. Barrarat, R. Karim, B. Helifa, I. Lefkaier, Characterization of subsurface cracks in eddy current testing using machine learning methods, Int. J. Numer. Modell. Electron. Netw. Devices Fields 35 (2021). https://doi.org/10.1002/jnm.2876

[31] R. Hamia, C. Cordier, C. Dolabdjian, Eddy-current non-destructive testing system for the determination of crack orientation, NDT E Int. 61 (2014) 24–28. https://doi.org/10.1016/j.ndteint.2013.09.005